



Publication Year	2021
Acceptance in OA	2022-07-20T10:42:27Z
Title	Trigonometric Parallaxes of Four Star-forming Regions in the Distant Inner Galaxy
Authors	Xu, Y., Bian, S. B., Reid, M. J., Li, J. J., Menten, K. M., Dame, T. M., Zhang, B., Brunthaler, A., Wu, Y. W., MOSCADELLI, Luca, Wu, G., Zheng, X. W.
Publisher's version (DOI)	10.3847/1538-4365/abd8cf
Handle	http://hdl.handle.net/20.500.12386/32527
Journal	THE ASTROPHYSICAL JOURNAL SUPPLEMENT SERIES
Volume	253



Trigonometric Parallaxes of Four Star-forming Regions in the Distant Inner Galaxy

Y. Xu¹, S. B. Bian^{1,2}, M. J. Reid³, J. J. Li¹, K. M. Menten⁴, T. M. Dame³, B. Zhang⁵, A. Brunthaler⁴,
Y. W. Wu⁶, L. Moscadelli⁷, G. Wu⁸, and X. W. Zheng⁹

¹ Purple Mountain Observatory, Chinese Academy of Sciences, Nanjing 210033, People's Republic of China; xuye@pmo.ac.cn

² School of Astronomy and Space Science, University of Science and Technology of China, Hefei 230026, People's Republic of China

³ Center for Astrophysics | Harvard & Smithsonian, 60 Garden Street, Cambridge, MA 02138, USA

⁴ Max-Planck-Institut für Radioastronomie, Auf dem Hügel 69, D-53121 Bonn, Germany

⁵ Shanghai Astronomical Observatory, Chinese Academy of Sciences, Shanghai 200030, People's Republic of China

⁶ National Time Service Center, Chinese Academy of Sciences, Xi'an 710600, People's Republic of China

⁷ INAF-Osservatorio Astrofisico di Arcetri, Largo E. Fermi 5, I-50125 Firenze, Italy

⁸ Xinjiang Astronomical Observatory, Chinese Academy of Sciences, Urumqi 830011, People's Republic of China

⁹ Nanjing University, Nanjing 20093, People's Republic of China

Received 2020 October 3; revised 2020 December 31; accepted 2021 January 4; published 2021 February 16

Abstract

We have measured trigonometric parallaxes for four H₂O masers associated with distant massive young stars in the inner regions of the Galaxy using the Very Long Baseline Array as part of the BeSSeL Survey. G026.50 + 0.28 is located at the near end of the Galactic bar, perhaps at the origin of the Norma spiral arm. G020.77–0.05 is in the Galactic Center region and is likely associated with a far-side extension of the Scutum arm. G019.60–0.23 and G020.08–0.13 are likely associated and lie well past the Galactic Center. These sources appear to be in the Sagittarius spiral arm, but an association with the Perseus arm cannot be ruled out.

Unified Astronomy Thesaurus concepts: Water masers (1790); Trigonometric parallax (1713); Star formation (1569); Milky Way Galaxy (1054)

1. Introduction

Mapping the Milky Way's spiral structure is a challenging enterprise, since distances can exceed 10 kpc and dust in the plane obscures optical light. The use of maser parallax measurements with very long baseline interferometry (Hachisuka et al. 2006; Xu et al. 2006) has allowed astronomers to determine far more precise distances. Recently, VERA Collaboration et al. (2020) published a compilation of astrometry results. Together with the National Radio Astronomy Observatory's Very Long Baseline Array (VLBA) key science project, through the Bar and Spiral Structure Legacy (BeSSeL) Survey, summarized in Reid et al. (2019), a total of more than 200 parallaxes and proper motions of maser sources have been measured. A significant portion of the spiral arms of the Milky Way have now been characterized (e.g., Choi et al. 2014; Wu et al. 2014, 2019; Sato et al. 2014; Reid et al. 2019), especially within 5 kpc of the Sun (Xu et al. 2013, 2016; Hodges 2016). However, for very distant regions of the Milky Way, especially toward the Galactic Center, a paucity of parallax measurements still limits our understanding of the Galactic spiral structure. In order to improve upon this, as part of the BeSSeL Survey, we present trigonometric parallaxes of four distant star-forming regions toward the inner Galaxy.

2. Observations and Analysis

We observed 22 GHz H₂O masers toward four star-forming regions over 16 epochs with the VLBA, under program BR210; each epoch consisted of a 7 hr track. We scheduled observations near the peaks of the sinusoidal parallax signature in R.A., since the amplitude of the decl. signature is considerably smaller. Calibration procedures followed our well-documented BeSSeL Survey (Reid et al. 2009).

The parallax and proper motion of each source were fitted simultaneously using the obtained data. We added “error floors” in quadrature to the formal position uncertainties to achieve post-fit

residuals with χ^2 per degree of freedom near unity for both coordinates. Since uncompensated tropospheric delay differences between the masers and the background quasars usually dominate the systematics, and these delay differences are essentially the same for all maser spots in a source, we conservatively inflated formal parallax errors by the square root of the number of maser spots used. Table 1 summarizes parallax and proper motion results. Additional details on observations and analysis are presented in Appendix A.

Since water masers in star-forming regions form in outflows with expansion velocities of typically tens of kilometers per second, assigning a V_{LSR} to the central star which excites the masers can be uncertain at the $\pm 10 \text{ km s}^{-1}$ level. Therefore, we instead adopt the V_{LSR} measured with dense molecular tracers (e.g., NH₃ and CH₃OH) for the associated molecular cloud.

Our distances to G019.60–0.23 and G020.08–0.13 resolve a long-standing controversy as to whether the sources are at their near kinematic distance (~ 4 kpc; Georgelin & Georgelin 1976; Petriella et al. 2013) or the far one (~ 13 kpc; Kolpak et al. 2003; Ranasinghe & Leahy 2018). Their parallax distances of $13.2^{+2.2}_{-1.7}$ kpc and $15.2^{+2.7}_{-2.0}$ kpc strongly favor the far distance. The kinematic distance of G020.77–0.05 is ~ 11.6 kpc (Urquhart et al. 2018) based on the H I self-absorption technique, but its parallax distance of $8.1^{+0.9}_{-0.8}$ kpc is much less, suggesting its luminosity is just half its previous estimate. For G026.50 + 0.28, its kinematic distance of ~ 6.3 kpc (Molinari et al. 1996; Qiu et al. 2012) agrees with the parallax distance of $6.3^{+0.5}_{-0.4}$ kpc.

3. Galactic Distribution

Since the major spiral arms of the Galaxy have long been known to produce fairly well-defined arcs and loops in 21 cm and CO longitude–velocity (l, v) diagrams, the BeSSeL project assigns maser sources to spiral arms based on their well-determined positions in such diagrams—even before their parallaxes are

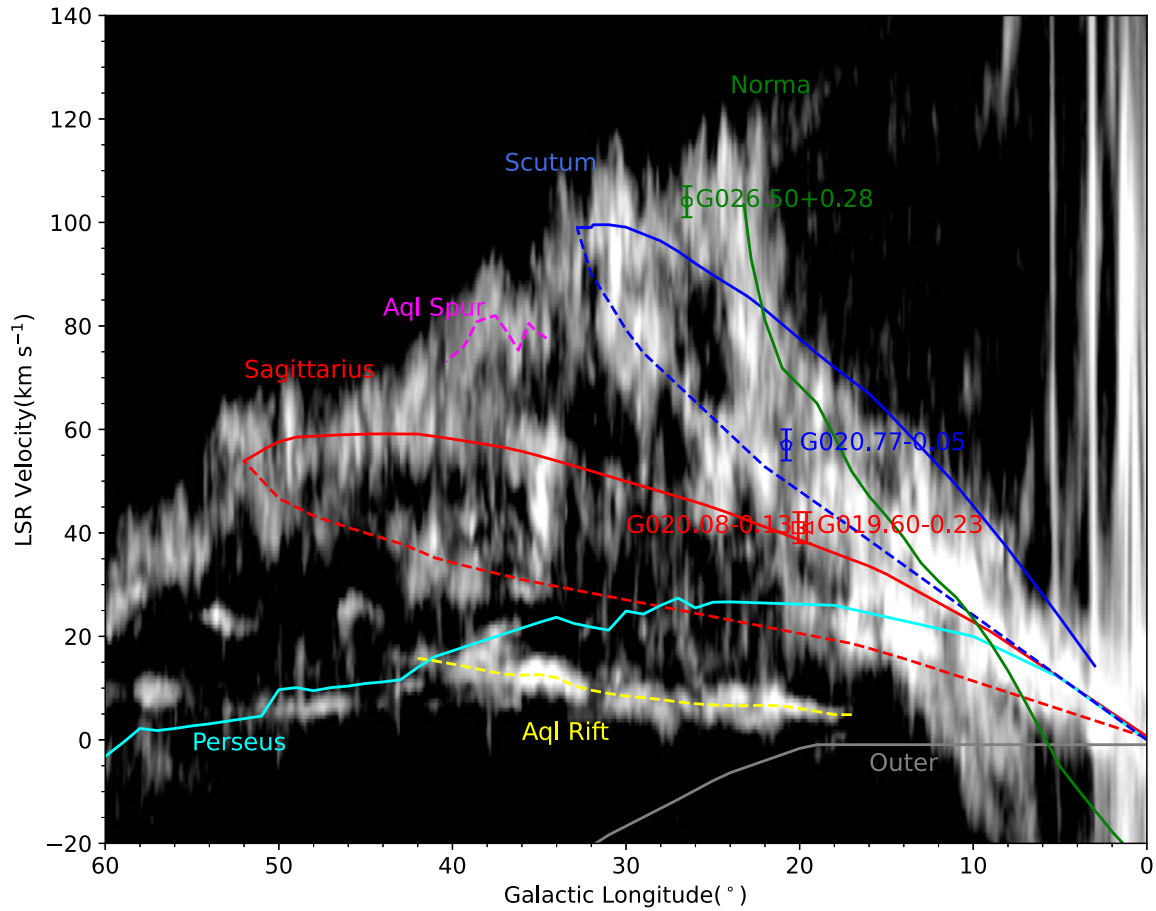


Figure 1. Location of masers superposed on a CO (l, v) diagram from Dame et al. (2001); the spiral arm traces are from Reid et al. (2016). Solid and dashed lines correspond to the near and far portions of arms interior to the solar circle. The CO (l, v) diagram is optimized to best display the intense inner-Galaxy arms, so the Perseus and Outer arms are not well represented here.

Table 1
Parallaxes and Proper Motions

Source	π (mas)	D (kpc)	μ_x (mas y ⁻¹)	μ_y (mas y ⁻¹)	V_{LSR}^* (km s ⁻¹)
G019.60–0.23	0.076 ± 0.011	$13.2^{+2.2}_{-1.7}$	-3.11 ± 0.16	-6.36 ± 0.17	$41^a \pm 3$
G020.08–0.13	0.066 ± 0.010	$15.2^{+2.7}_{-2.0}$	-3.14 ± 0.14	-6.44 ± 0.16	$41^b \pm 3$
G020.77–0.05	0.124 ± 0.013	$8.1^{+0.9}_{-0.8}$	-3.27 ± 0.26	-6.55 ± 0.27	$57^a \pm 3$
G026.50 + 0.28	0.159 ± 0.012	$6.3^{+0.5}_{-0.4}$	-2.51 ± 0.34	-6.04 ± 0.34	$104^c \pm 3$

Notes. Column 1 gives the Galactic source name/coordinates. Columns 2–5 give the parallax, parallax distance, and proper motion in the eastward ($\mu_x = \mu_\alpha \cos \delta$) and northward directions ($\mu_y = \mu_\delta$). Column 6 lists the local standard of rest velocity from molecular line emission.

^a Wienen et al. (2012), $\text{NH}_3(J, K) = (1, 1)$.

^b Dunham et al. (2011), $\text{NH}_3(J, K) = (1, 1)$.

^c Yang et al. (2017), CH_3OH .

measured. Figure 1 shows traces of the spiral arms in a CO (l, v) diagram of the first Galactic quadrant, with the positions of the present four maser sources overlaid. Figure 2 shows the same four sources as green polygons on the plane of the Galaxy along with the 200 maser parallax measurements (circles) from Reid et al. (2019). The error bars represent 1σ distance uncertainties.

Since the sources G019.60–0.23 and G020.08–0.13 have the same velocity and are separated by less than half a degree in the sky, it seems likely that they are physically associated. Judging from Figure 1, both appear to be in the Sagittarius arm, although an association with the Perseus arm cannot be ruled

out. This is especially true since it is difficult to determine the (l, v) locus of the distant Perseus arm in this very crowded section of the diagram (see Figure 8 in Reid et al. 2016). As shown in Figure 2, our parallax distances are likewise consistent with both sources being in the Sagittarius arm, although judging from this figure alone the Perseus arm is favored. Although G020.08–0.13 falls almost exactly on the Outer arm in Figure 2, an association with that arm can be confidently ruled out based on the velocity separation of 43 km s^{-1} between this source and the Outer arm locus in Figure 1. If both sources lie in the Sagittarius arm, they hint at

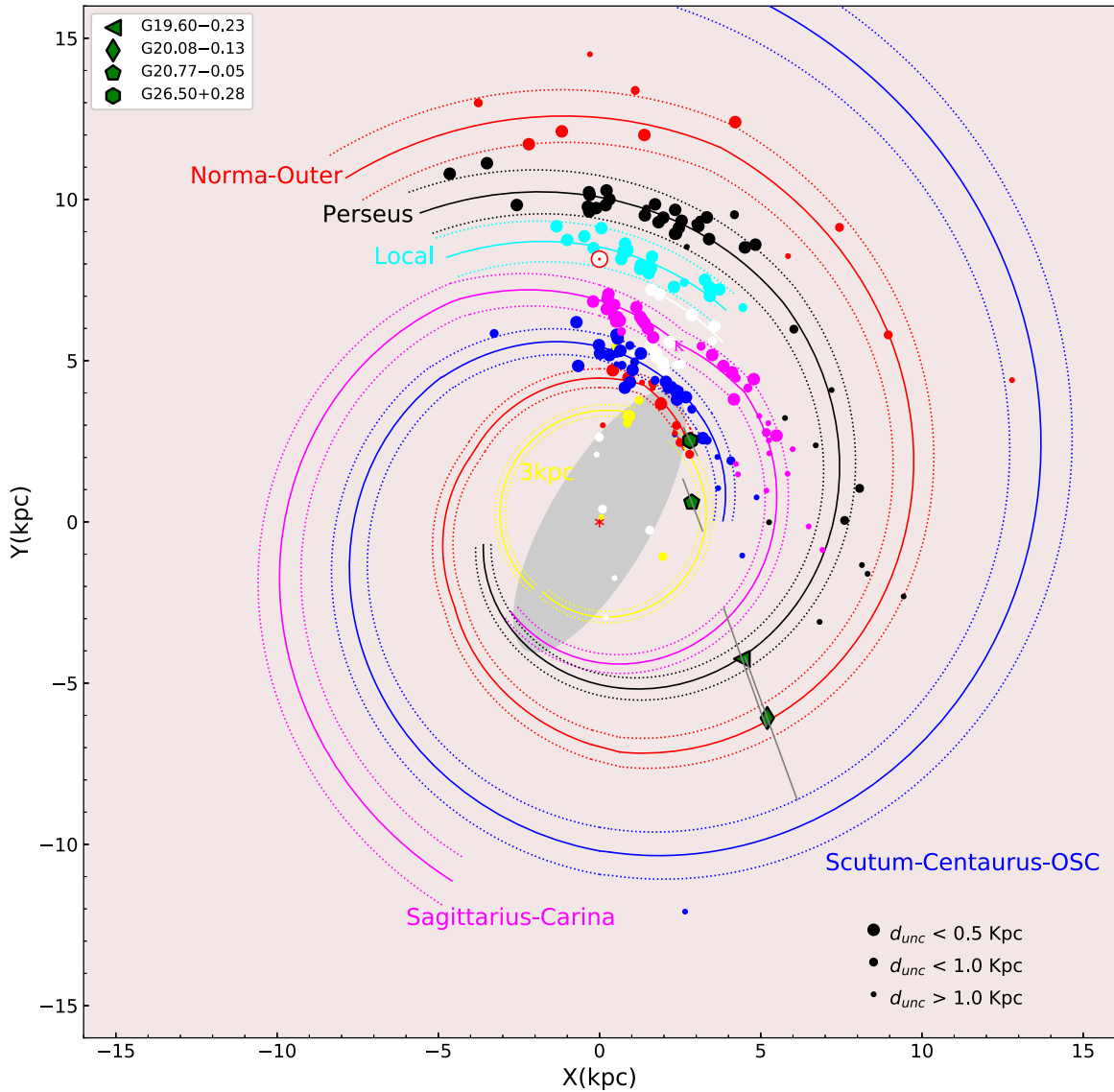


Figure 2. Plan view of the Milky Way from the north Galactic pole after Reid et al. (2019). The four sources reported in this paper are indicated with green polygons (see the legend in the upper left corner) with 1σ distance errors indicated. Locations of maser sources with previously measured parallaxes are indicated with solid dots. White dots indicate sources for which the arm assignments are unclear. Solid curved lines trace the centers of spiral arm models from Reid et al. (2019), and the dotted lines enclose 90% of the sources.

the need for a modification of the spiral arm fit shown in Figure 2, with the arm moving slightly farther out and perhaps even merging with the Perseus arm at low Galactic longitudes. However, tighter distance errors on these sources and others will be required before such an adjustment can be confirmed.

G020.77–0.05 presents an interesting case. Its (l, v) position in Figure 1 places it in the near side of the Scutum arm, but its parallax distance places it much closer to an extension of that arm on the far side (Figure 2). These two results can be reconciled if the source has a velocity anomalously low by about 20 km s^{-1} . This is entirely possible given the small Galactic radius of the source and its proximity to the end of the Galactic bar. Indeed, as discussed below, this source has very large peculiar motions in the plane of the Galaxy. Based on these findings, we tentatively suggest that the far portion of the Scutum arm extends from a Galactic longitude of 25° (corresponding to a Galactic azimuth of 90°) down to at least a longitude of 20° (azimuth 100°). However, we caution that the

Norma arm could also be a candidate for extension, and the Norma and Scutum arms may even merge there. Clearly more parallax measurements are needed to untangle these possibilities.

G026.50 + 0.28 is in a very crowded region of the inner Galaxy. Its (l, v) position is consistent with both the near side of the Norma arm and the far side of the Scutum arm. Our parallax distance of $6.3^{+0.5}_{-0.4} \text{ kpc}$ resolves this choice in favor of Norma. The source is located near the end of the bar, where a large number of high mass star-forming regions are known to exist. Likely, the gravitational potential of the galactic bar accumulates dust and gas there and intensifies the star-forming activity.

We calculate the peculiar (noncircular) motions for these four sources using the methodology described in Reid et al. (2009) with the Galactic model and solar motion of Reid et al. (2019). The results are listed in Table 2. For G019.60–0.23 and G020.08–0.13, the peculiar motions are consistent with U_s and W_s magnitudes $\lesssim 10 \text{ km s}^{-1}$; the uncertainties in the V_s

Table 2
Peculiar Motions

Source	U_s (km s^{-1})	V_s (km s^{-1})	W_s (km s^{-1})
G019.60–0.23	-12 ± 8	7 ± 63	-5 ± 11
G020.08–0.13	-13 ± 6	74 ± 85	-8 ± 11
G020.77–0.05	31 ± 16	-56 ± 12	2 ± 10
G026.50 + 0.28	34 ± 15	-14 ± 5	-8 ± 10

Note. The Galactic “Univ” model and solar motion found by Reid et al. (2019) were used to calculate the peculiar motions.

values are too large for meaningful analysis. These large V_s uncertainties can be traced to a large motion in Galactic longitude scaled by their Galactocentric radii. These radii have ± 2 kpc uncertainties, as their parallax distance uncertainties map almost directly to radii. This is discussed in detail in Appendix B.

Both G020.77–0.05 and G026.50 + 0.28 appear to have some very large peculiar motions in the plane of the Galaxy. They have motions toward the Galactic center (U_s) of about 30 km s^{-1} , and these are significant at the 2σ level. Formally, G020.77–0.05 has a peculiar component of 56 km s^{-1} counter to Galactic rotation. However, this estimate is dependent on extrapolation of the “universal” rotation curve fitted to sources with Galactic radii > 4 kpc. Either G020.77–0.05 is orbiting the Galaxy considerably slower than indicated by the rotation curve, indicating a significantly elliptical orbit, and/or the rotation curve is a too simplistic model for this region.

4. Summary

In order to extend our knowledge of the distances to sources in the distant regions of the Milky Way, we measured the parallaxes and proper motions of four masers associated with massive young stars. The results of G019.60–0.23 and G020.08–0.13 hint at a modification of the Sagittarius arm model of Reid et al. (2019). Near the Galactic bar, many sources (G020.77–0.05, G026.50 + 0.28 and others in Immer et al. 2019) have significant noncircular motions, suggesting the bar’s strong gravitational potential has a significant effect.

This work was supported by the National Natural Science Foundation of China (grant Nos. 11933011, 11873019, and 11673066), the Key Laboratory for Radio Astronomy, Project of Xinjiang Uygur Autonomous Region of China for Flexibly Fetching in Upscale Talents, and Heaven Lake Hundred-Talent Program of Xinjiang Uygur Autonomous Region of China.

Facility: VLBA.

Appendix A

Here, we show the details of the epochs observed (Table 3), observational parameters (Table 4), and parallax fits of the individual sources (Table 5 and Figure 3). The uncertainties of parallaxes and proper motions given in Table 5 are the formal fitting uncertainties.

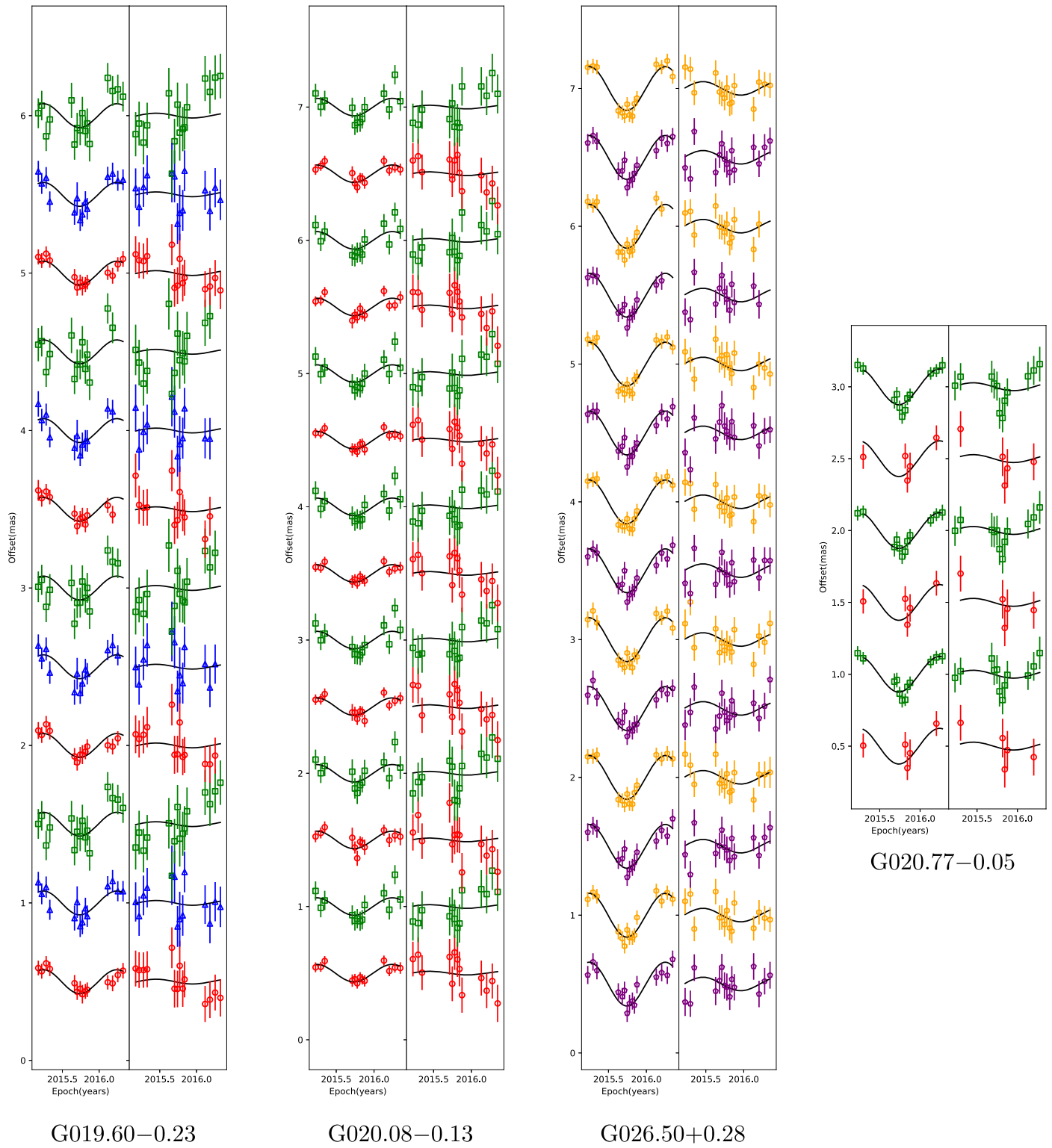


Figure 3. Results for the combined parallax fit of G019.60-0.23, G020.08-0.13, G020.77-0.05, and G026.50 + 0.28. The left and right panels are combined parallax fit curves (black) in R.A. and decl. directions, respectively. Different marks indicate different background sources: red circles (J1821-1224), blue triangles (J1835-1248), green squares (J1835-1115), purple pentagons (J1833-0323), and orange hexagons (J1846-0651).

Table 3
Details of the Epochs Observed

Epoch	Source	Source	Source	Source
E1	G019.60–0.23 2015 Mar 5	G020.08–0.13	G020.77–0.05	G026.50+0.28
E2	2015 Mar 22	2015 Mar 25	2015 Mar 25	2015 Mar 25
E3	2015 Apr 13	2015 Apr 19	2015 Apr 19	2015 Apr 19
E4	2015 May 1	2015 May 8	2015 May 8	2015 May 8
E5	2015 Aug 18	2015 Aug 19	2015 Aug 19	2015 Aug 19
E6	2015 Sep 1	2015 Sep 7	2015 Sep 7	2015 Sep 7
E7	2015 Sep 14	2015 Sep 18	2015 Sep 18	2015 Sep 18
E8	2015 Sep 29	2015 Oct 1	2015 Oct 1	2015 Oct 1
E9	2015 Oct 10	2015 Oct 12	2015 Oct 12	2015 Oct 12
E10	2015 Oct 25	2015 Oct 26	2015 Oct 26	2015 Oct 26
E11	2015 Nov 3	2015 Nov 5	2015 Nov 5	2015 Nov 5
E12	2015 Nov 15	2015 Nov 17	2015 Nov 17	2015 Nov 17
E13	2016 Feb 13	2016 Feb 18	2016 Feb 18	2016 Feb 18
E14	2016 Mar 8	2016 Mar 15	2016 Mar 15	2016 Mar 15
E15	2016 Apr 3	2016 Apr 11	2016 Apr 11	2016 Apr 11
E16	2016 Apr 29	2016 May 7	2016 May 7	2016 May 7

Table 4
Positions and Brightnesses

Source	R.A. (J2000) (^h ^m ^s)	Decl. (J2000) ([°] ['] ["])	ϕ ([°])	Brightness (Jy beam ⁻¹)	V_{LSR} (km s ⁻¹)	NW beam (mas, mas, deg)
G019.60–0.23	18 27 38.0737	–11 56 37.558		23.1	24.84	2.0 × 1.1 @ 18
J1821–1224	18 21 23.27806	–12 24 12.9282	1.6	0.023		2.3 × 1.1 @ 16
J1835–1248	18 35 58.07853	–12 48 51.5492	2.2	0.013		2.2 × 1.2 @ 15
J1835–1115	18 35 19.57583	–11 15 59.3116	2.0	0.026		2.1 × 1.2 @ 15
G020.08–0.13	18 28 10.2867	–11 28 47.892		7.8	46.43	1.7 × 0.4 @ –18
J1821–1224	18 21 23.27806	–12 24 12.9284	1.9	0.013		1.7 × 0.4 @ –18
J1835–1115	18 35 19.57583	–11 15 59.3116	1.8	0.015		1.8 × 0.4 @ –19
G020.77–0.05	18 29 11.5819	–10 49 58.566		1.9	58.60	1.9 × 1.0 @ 15
J1821–1224	18 21 23.27806	–12 24 12.9287	2.5	0.007		2.0 × 1.0 @ 14
J1835–1115	18 35 19.57583	–11 15 59.3116	1.6	0.017		1.9 × 1.0 @ 16
G026.50 + 0.28	18 38 40.7518	–05 35 05.108		14.8	104.11	2.4 × 1.1 @ 38
J1846–0651	18 46 06.30026	–06 51 27.7462	2.2	0.031		2.4 × 1.0 @ 37
J1833–0323	18 33 23.90488	–3 23 31.4442	2.6	0.035		2.3 × 1.0 @ 40

Note. ϕ is the angular separation between a maser and its calibrator. The maser's absolute position, peak brightness, size, and position angle, measured from north to east, of the naturally weighted (NW) beam are listed for the first/second epoch for each source. V_{LSR} is the velocity of the phase-reference channel.

Table 5
Detailed Results of the Parallaxes and Proper Motions of Masers

Background Source	V_{LSR} (km s $^{-1}$)	Detected Epochs	Parallax (mas)	μ_x (mas y $^{-1}$)	μ_y (mas y $^{-1}$)	Δx (mas)	Δy (mas)
G019.60–0.23							
J1821–1224	24.84	1111 01111110 1111	0.059 ± 0.008	−2.99 ± 0.02	−6.62 ± 0.04	0	0
	38.75	1111 01111110 1111	0.071 ± 0.009	−3.09 ± 0.02	−6.49 ± 0.04	−679.513 ± 0.012	835.549 ± 0.017
	42.20	1111 01111110 1100	0.061 ± 0.010	−3.35 ± 0.03	−6.87 ± 0.10	−986.537 ± 0.046	869.388 ± 0.078
	43.82	1111 01111110 1110	0.058 ± 0.010	−3.28 ± 0.03	−6.20 ± 0.06	−1121.819 ± 0.025	1113.290 ± 0.037
	Combined fit		0.062 ± 0.009				
J1835–1248	24.84	1111 01111110 1111	0.092 ± 0.017	−2.89 ± 0.04	−6.49 ± 0.08	0	0
	38.75	1111 01111110 1111	0.103 ± 0.017	−3.00 ± 0.04	−6.35 ± 0.07	−679.513 ± 0.012	835.549 ± 0.017
	42.20	1111 01111110 1100	0.107 ± 0.021	−3.18 ± 0.06	−6.72 ± 0.10	−986.537 ± 0.046	869.388 ± 0.078
	43.82	1111 01111110 1110	0.098 ± 0.019	−3.17 ± 0.05	−6.05 ± 0.09	−1121.819 ± 0.025	1113.290 ± 0.037
	Combined fit		0.100 ± 0.018				
J1835–1115	24.84	1111 11111111 1111	0.077 ± 0.023	−2.75 ± 0.06	−6.11 ± 0.07	0	0
	38.75	1111 11111111 1111	0.085 ± 0.025	−2.86 ± 0.06	−5.98 ± 0.09	−679.513 ± 0.012	835.549 ± 0.017
	42.20	1111 11111111 1100	0.093 ± 0.034	−3.05 ± 0.10	−6.40 ± 0.13	−986.537 ± 0.046	869.388 ± 0.078
	43.82	1111 11111111 1110	0.090 ± 0.024	−3.01 ± 0.07	−5.72 ± 0.10	−1121.819 ± 0.025	1113.290 ± 0.037
	Combined fit		0.086 ± 0.025				
Combined fit 2			0.076 ± 0.011				
Average				−3.11 ± 0.03	−6.36 ± 0.06		
G020.08–0.13							
J1821–1224	47.29	111 00111111 1111	0.049 ± 0.013	−3.24 ± 0.03	−6.34 ± 0.10	0.698 ± 0.019	27.929 ± 0.038
	46.43	111 00111111 1111	0.057 ± 0.009	−3.37 ± 0.02	−6.79 ± 0.08	0	0
	42.44	111 00111111 1111	0.061 ± 0.014	−3.04 ± 0.03	−6.69 ± 0.08	210.409 ± 0.007	30.584 ± 0.018
	41.58	111 00111111 1111	0.059 ± 0.012	−3.11 ± 0.03	−6.67 ± 0.07	208.070 ± 0.009	31.209 ± 0.021
	40.50	111 00111111 1111	0.054 ± 0.009	−3.06 ± 0.02	−6.67 ± 0.08	210.415 ± 0.002	29.216 ± 0.004
	39.85	111 00111111 1111	0.062 ± 0.009	−3.03 ± 0.02	−6.86 ± 0.08	−415.336 ± 0.002	−157.077 ± 0.005
	37.05	111 00111111 1111	0.063 ± 0.012	−3.22 ± 0.03	−6.59 ± 0.09	6.160 ± 0.013	−274.918 ± 0.028
	Combined fit		0.058 ± 0.011				
J1835–1115	47.29	111 00111111 1111	0.084 ± 0.024	−3.19 ± 0.06	−5.87 ± 0.10	0.698 ± 0.019	27.929 ± 0.038
	46.43	111 00111111 1111	0.089 ± 0.022	−3.31 ± 0.06	−6.30 ± 0.08	0	0
	42.44	111 00111111 1111	0.095 ± 0.021	−2.98 ± 0.05	−6.21 ± 0.09	210.409 ± 0.007	30.584 ± 0.018
	41.58	111 00111111 1111	0.089 ± 0.023	−3.05 ± 0.06	−6.19 ± 0.08	208.070 ± 0.009	31.209 ± 0.021
	40.50	111 00111111 1111	0.087 ± 0.022	−3.00 ± 0.06	−6.18 ± 0.08	210.415 ± 0.002	29.216 ± 0.004
	39.85	111 00111111 1111	0.095 ± 0.021	−2.97 ± 0.05	−6.38 ± 0.08	−415.336 ± 0.002	−157.077 ± 0.005
	37.05	111 00111111 1111	0.097 ± 0.022	−3.16 ± 0.06	−6.11 ± 0.07	6.160 ± 0.013	−274.918 ± 0.028
	Combined fit		0.091 ± 0.021				
Combined fit 2			0.066 ± 0.010				
Average				−3.14 ± 0.02	−6.44 ± 0.08		
G020.77–0.05							
J1821–1224	58.60	010 00000111 0100	0.094 ± 0.047	−3.37 ± 0.14	−6.57 ± 0.17	0	0
	60.32	010 00000111 0100	0.093 ± 0.049	−2.75 ± 0.14	−7.10 ± 0.21	358.791 ± 0.010	−203.425 ± 0.017
	62.05	010 00000111 0100	0.085 ± 0.052	−3.25 ± 0.15	−6.82 ± 0.19	193.117 ± 0.014	−112.847 ± 0.023
	Combined fit		0.091 ± 0.043				
J1835–1115	58.60	110 01111111 1110	0.127 ± 0.015	−3.55 ± 0.04	−6.24 ± 0.08	0	0
	60.32	110 01111111 1110	0.135 ± 0.014	−2.91 ± 0.04	−6.74 ± 0.11	358.791 ± 0.010	−203.425 ± 0.017
	62.05	110 01111111 1110	0.123 ± 0.011	−3.40 ± 0.03	−6.45 ± 0.09	193.117 ± 0.014	−112.847 ± 0.023
	Combined fit		0.129 ± 0.013				
Combined fit 2			0.124 ± 0.013				
Average				−3.27 ± 0.04	−6.55 ± 0.08		
G026.50 + 0.28							
J1833–0323	96.88	111 11111111 1111	0.136 ± 0.015	−2.99 ± 0.04	−6.05 ± 0.08	−462.539 ± 0.008	1161.731 ± 0.019
	101.84	111 11111111 1111	0.135 ± 0.018	−2.30 ± 0.05	−5.91 ± 0.08	−51.324 ± 0.018	955.927 ± 0.041
	102.49	111 11111111 1100	0.138 ± 0.015	−2.33 ± 0.05	−5.64 ± 0.11	149.468 ± 0.010	989.235 ± 0.022
	102.92	111 11111111 1111	0.152 ± 0.016	−2.37 ± 0.04	−5.79 ± 0.09	−38.638 ± 0.013	936.896 ± 0.030
	104.76	111 11111111 1111	0.137 ± 0.015	−2.52 ± 0.04	−5.55 ± 0.08	129.780 ± 0.028	1010.760 ± 0.056
	106.59	111 11111111 1111	0.117 ± 0.017	−2.76 ± 0.05	−6.87 ± 0.07	607.880 ± 0.014	693.811 ± 0.029
	107.13	111 11111111 1111	0.130 ± 0.017	−2.36 ± 0.05	−5.81 ± 0.08	160.330 ± 0.012	973.750 ± 0.029
	Combined fit		0.135 ± 0.016				

Table 5
(Continued)

Background Source	V_{LSR} (km s ⁻¹)	Detected Epochs	Parallax (mas)	μ_x (mas y ⁻¹)	μ_y (mas y ⁻¹)	Δx (mas)	Δy (mas)
J1846–0651	96.88	111 11111111 1111	0.175 ± 0.011	-2.98 ± 0.03	-6.23 ± 0.06	-462.539 ± 0.008	1161.731 ± 0.019
	101.84	111 11111111 1111	0.175 ± 0.010	-2.29 ± 0.03	-6.08 ± 0.06	-51.324 ± 0.018	955.927 ± 0.041
	102.49	111 11111111 1100	0.186 ± 0.016	-2.27 ± 0.05	-5.85 ± 0.09	149.468 ± 0.010	989.235 ± 0.022
	102.92	111 11111111 1111	0.189 ± 0.011	-2.36 ± 0.03	-5.98 ± 0.07	-38.638 ± 0.013	936.896 ± 0.030
	104.76	111 11111111 1111	0.177 ± 0.013	-2.50 ± 0.04	-5.72 ± 0.08	129.780 ± 0.028	1010.760 ± 0.056
	106.59	111 11111111 1111	0.157 ± 0.013	-2.74 ± 0.04	-7.05 ± 0.07	607.880 ± 0.014	693.811 ± 0.029
	107.13	111 11111111 1111	0.172 ± 0.010	-2.34 ± 0.03	-5.99 ± 0.07	160.330 ± 0.012	973.750 ± 0.029
	Combined fit			0.176 ± 0.012			
Combined fit 2			0.159 ± 0.012				
Average				-2.51 ± 0.03	-6.04 ± 0.06		

Note. In combined fit 2, we put all the data in the fitting program and combine the individual error floors with the JMFIT values in the data files.

Appendix B

Here we combine the steps documented in Reid et al. (2009) to obtain source peculiar motions: U_s (toward the Galactic Center), V_s (in the direction of Galactic rotation), W_s (toward the north Galactic pole).

$$\begin{aligned}
 U_s = & v_{\text{Helio}} \cos b \cos(\ell + \beta) \\
 & - D\mu_b \sin b \cos(\ell + \beta) \\
 & - D\mu_\ell \cos b \sin(\ell + \beta) \\
 & - (V_\odot + \Theta_0) \sin \beta \\
 & + U_\odot \cos \beta,
 \end{aligned}$$

$$\begin{aligned}
 V_s = & v_{\text{Helio}} \cos b \sin(\ell + \beta) \\
 & - D\mu_b \sin b \sin(\ell + \beta) \\
 & + D\mu_\ell \cos b \cos(\ell + \beta) \\
 & + (V_\odot + \Theta_0) \cos \beta \\
 & + U_\odot \sin \beta \\
 & - \Theta_s,
 \end{aligned}$$

$$W_s = (D\mu_b \cos b + v_{\text{Helio}} \sin b + W_\odot),$$

where v_{Helio} is the heliocentric radial velocity. μ_ℓ and μ_b are proper motions in Galactic longitude (ℓ) and latitude (b) (converted from those measured in the eastward and northward directions); β is the Galactocentric azimuth (defined as 0 toward the Sun and increasing in the direction of Galactic rotation); ($U_\odot, V_\odot + \Theta_0, W_\odot$) describe the noncircular motion of the Sun; Θ_s is the rotation speed of the Galaxy at the source, and D is its distance from the Sun.

Using the following relations

$$\begin{aligned}
 \frac{\sin(\ell + \beta)}{R_0} &= \frac{\sin \beta}{D_p}, \\
 R_s &= -D_p \cos(\ell + \beta) + R_0 \cos \beta,
 \end{aligned}$$

where $D_p = D \cos b$, and R_0 and R_s are the Galactocentric radii of the Sun and the sources, we obtain $D\mu_\ell \cos b \sin(\ell + \beta) = \mu_\ell R_0 \sin \beta$, $D\mu_b \cos b \cos(\ell + \beta) = \mu_b (R_0 \cos \beta - R_s)$.

Then,

$$\begin{aligned}
 U_s = & v_{\text{Helio}} \cos b \cos(\ell + \beta) \\
 & - D\mu_b \sin b \cos(\ell + \beta) \\
 & - (\mu_\ell R_0 + V_\odot + \Theta_0) \sin \beta \\
 & + U_\odot \cos \beta,
 \end{aligned} \tag{1}$$

$$\begin{aligned}
 V_s = & v_{\text{Helio}} \cos b \sin(\ell + \beta) \\
 & - D\mu_b \sin b \sin(\ell + \beta) \\
 & + (\mu_\ell R_0 + V_\odot + \Theta_0) \cos \beta - \mu_\ell R_s \\
 & + U_\odot \sin \beta \\
 & - \Theta_s.
 \end{aligned} \tag{2}$$

For G019.60–0.23 and G020.08–0.13, uncertainties in the measured motions and distances lead to terms of $\sim 10 \text{ km s}^{-1}$ for U_s in Equation (1). However, for V_s the term $\mu_\ell R_s$ can contribute to a substantial uncertainty of

$$\sigma^2 = R_s^2 \sigma_{\mu_\ell}^2 + \mu_\ell^2 \sigma_{R_s}^2,$$

dominated by the second term containing $\sigma_{R_s}^2$. For $\mu_\ell \approx 7.2 \text{ mas y}^{-1}$ and $\sigma_{R_s} \approx 2 \text{ kpc}$, this leads to an uncertainty of $\sigma \approx 70 \text{ km s}^{-1}$.

ORCID iDs

Y. Xu  <https://orcid.org/0000-0001-5602-3306>
S. B. Bian  <https://orcid.org/0000-0002-7508-9615>
M. J. Reid  <https://orcid.org/0000-0001-7223-754X>
K. M. Menten  <https://orcid.org/0000-0001-6459-0669>
T. M. Dame  <https://orcid.org/0000-0003-0109-2392>
B. Zhang  <https://orcid.org/0000-0003-1353-9040>
A. Brunthaler  <https://orcid.org/0000-0003-4468-761X>
Y. W. Wu  <https://orcid.org/0000-0003-3188-5983>

References

- Choi, Y. K., Hachisuka, K., Reid, M. J., et al. 2014, *ApJ*, 790, 99
Dame, T. M., Hartmann, D., & Thaddeus, P. 2001, *ApJ*, 547, 792
Dunham, M. K., Rosolowsky, E., Evans, N. J., et al. 2011, *ApJ*, 741, 110
Georgelin, Y. M., & Georgelin, Y. P. 1976, *A&A*, 49, 57
Hachisuka, K., Brunthaler, A., Menten, K. M., et al. 2006, *ApJ*, 645, 337
Hodges, K. V. 2016, *Sci*, 353, 1509
Immer, K., Li, J., Quiroga-Nuñez, L. H., et al. 2019, *A&A*, 632, 123
Kolpak, M. A., Jackson, J. M., Bania, T. M., et al. 2003, *ApJ*, 582, 756
Molinari, S., Brand, J., Cesaroni, R., et al. 1996, *A&A*, 308, 573

- Petriella, A., Paron, S. A., & Giacani, E. B. 2013, [A&A](#), **554**, A73
- Qiu, K., Zhang, Q., Beuther, H., et al. 2012, [ApJ](#), **756**, 170
- Ranasinghe, S., & Leahy, D. A. 2018, [AJ](#), **155**, 204
- Reid, M. J., Dame, T. M., Menten, K. M., et al. 2016, [ApJ](#), **823**, 77
- Reid, M. J., Menten, K. M., Brunthaler, A., et al. 2019, [ApJ](#), **885**, 131
- Reid, M. J., Menten, K. M., Zheng, X. W., et al. 2009, [ApJ](#), **700**, 137
- Sato, M., Wu, Y. W., Immer, K., et al. 2014, [ApJ](#), **793**, 72
- Urquhart, J. S., König, C., Giannetti, A., et al. 2018, [MNRAS](#), **473**, 1059
- VERA Collaboration, Hirota, T., Nagayama, T., et al. 2020, [PASJ](#), **72**, 50
- Wienen, M., Wyrowski, F., Schuller, F., et al. 2012, [A&A](#), **544**, A146
- Wu, Y. W., Reid, M. J., Sakai, N., et al. 2019, [ApJ](#), **874**, 94
- Wu, Y. W., Sato, M., Reid, M. J., et al. 2014, [A&A](#), **566**, A17
- Xu, Y., Li, J. J., Reid, M. J., et al. 2013, [ApJ](#), **769**, 15
- Xu, Y., Reid, M., Dame, T., et al. 2016, [SciA](#), **2**, e1600878
- Xu, Y., Reid, M. J., Zheng, X. W., & Menten, K. M. 2006, [Sci](#), **311**, 54
- Yang, W., Xu, Y., Chen, X., et al. 2017, [ApJS](#), **231**, 20